Chatoyant: a computer-aided-design tool for free-space optoelectronic systems

Steven P. Levitan, Timothy P. Kurzweg, Philippe J. Marchand, Mark A. Rempel, Donald M. Chiarulli, Jose A. Martinez, John M. Bridgen, Chi Fan, and Frederick B. McCormick

Chatoyant is a tool for the simulation and the analysis of heterogeneous free-space optoelectronic architectures. It is capable of modeling digital and analog electronic and optical signal propagation with mechanical tolerancing at the system level. We present models for a variety of optoelectronic devices and results that demonstrate the system's ability to predict the effects of various component parameters, such as detector geometry, and system parameters, such as alignment tolerances, on system-performance measures, such as the bit-error rate.

OCIS codes: 200.0200, 220.0220, 220.4830, 250.0250.

1. Introduction

Free-space (FS) optoelectronic (OE) information-processing systems are key components of the next generation of computers and communications networks. Currently the state of the art for design and analysis of these systems is to use a set of *ad hoc* procedures to generate end-to-end system-performance estimates based on empirical characterizations of the component devices. This painstaking technique results in rough approximations, which must then be refined by an actual prototype of each of the particular systems under consideration. As a result, although many systems have been proposed, few FS OE systems have been designed, and fewer still have been built. This is in sharp contrast to the growth of rapid prototypical systems in the electronic (VLSI) domain, in which the path from concept to system is often as short as a few weeks.

The reasons for this problem become clear when we look at an example of a simple OE system. Figure 1 shows a system consisting of a digital logic module interfaced to a modulator array that supports parallel information channels. These are switched by a spatial light modulator and directed to a detector array, where the channels are received and passed on to another digital subsystem. The two digital subsystems could be composed of simple logic modules or could be as complex as an array of processing elements (i.e., CPU's), making the system a tightly coupled parallel processor. In this case the optoelectronics would provide high-bandwidth channels between the processors. Over the past decade many hybrid systems of this type have been proposed for applications as diverse as multistage interconnection networks, crossbar switches, intelligent optical backplanes, optical neural systems, three-dimensional digital optical computers, and analog optical processors.[1–4]

The design of these complex systems has been impeded because currently there are no complete OE system-level modeling tools. To address this need, we have created Chatoyant, a design framework and simulation tool that uses system-level models of OE components. The framework provides bridges to existing specialized tools with analysis filters to sort and aggregate their results. The simulation tool provides system-level simulation and analysis for OE devices (e.g., sources and detectors) with a high-level optical system simulator based on Gaussian beam propagation.

To date, there has been some research on computer-aided-design (CAD) systems exclusively for fiber networks.[5] Other researchers have focused on mechanical issues.[6] Also, several researchers have

S. P. Levitan, T. P. Kurzweg, M. A. Rempel, J. A. Martinez, and J. M. Bridgen are with the Department of Electrical Engineering and D. M. Chiarulli is with the Department of Computer Science, University of Pittsburgh, Pittsburgh, Pennsylvania 15261. P. J. Marchand and C. Fan are with the Department of Electrical and Computer Engineering, University of California, San Diego, La Jolla, California 92093. F. B. McCormick is with Call/Recall, Inc., 6160 Lusk Boulevard, Suite C-206, San Diego, California 92121.

Received 19 November 1997; revised manuscript received 20 February 1998.

0003-6935/98/266078-15$15.00/0

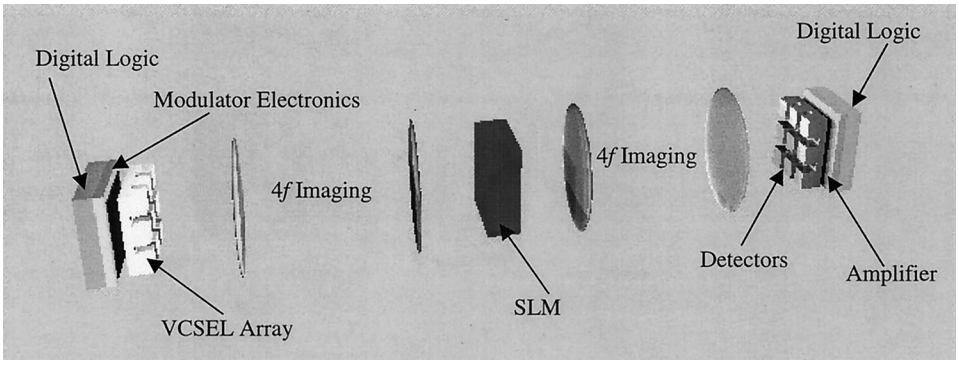

Fig. 1. FS OE system: VCSEL, vertical-cavity surface-emitting laser; SLM, spatial light modulator.

proposed implementing system-level tools by extending an existing simulation language such as VHDL[7–9] or SPICE[10,11] or by using a prototypical microelectronics CAD tool such as Genesys.[12] Other groups have built their research on extending signal-propagation models[13,14] or device models.[15,16] The problems with these techniques come from the limitations imposed by attempts to extend existing tools beyond their original capabilities. It is difficult to generalize these tools successfully for a wide range of OE system-level concerns.

An important distinction needs to be made between the functional *simulation* that Chatoyant performs and the more abstract performance or parametric *analysis* provided by other techniques. Chatoyant provides system-level end-to-end simulations of the computation performed by the system by use of actual data values provided by the user as well as ensemble performance information on speed, power, the bit-error rate (BER), etc.[17]

The rest of this paper is organized as follows. We first discuss the issues involved in OE system design. We then give some examples of our models for OE signals and components that are appropriate for both static and dynamic system-level simulation. Finally, we present results from simulations of several simple systems and show how Chatoyant can be used to perform technological and architectural trade-offs. We conclude with our plans for future research.

2. Optoelectronic System Design

The design of OE systems encompasses the traditional concerns of complex digital electronic systems such as decomposition, functionality, performance, and cost. As in analog design, it must also include explicit input–output analysis of the components at each level of the decomposition hierarchy. Additionally, OE system design must define the appropriate technology, from among electronic, optical, and packaging choices, for each component. After those decisions are made the components themselves can be refined.

These issues are summarized in Fig. 2. The figure shows how OE system design incorporates a number of design disciplines, shown horizontally, from electronics to mechanical tolerancing. It also shows various levels of abstraction in each discipline, shown vertically, from the higher or abstract system levels to more detailed component and device levels of analysis and simulation. On the right-hand side of Fig. 2 we show the corresponding levels of simulation and analysis, from higher to lower, for which the trade-offs for analysis tools are in terms of accuracy versus computation time.

Figure 2 also shows how Chatoyant supports the design flow for such mixed-technology OE systems with the ability to provide simulation and analysis at the OE system level. At this level modeling and analysis of complete subsystems allow the designer to perform design trade-offs in terms of both technology and architecture. This enables a system architect to perform truly systemwide what-if analyses rather than merely analyze a subset of the system constraints.

On the left-hand side of Fig. 2 we show the relation of top-down and bottom-up design decisions, for which analysis from the lower levels allows the designer to make design choices at the higher levels, or, conversely, for which design questions at the higher levels can be pushed down to lower levels for detailed analysis. This is provided for in Chatoyant by use of parameterized component models, created by use of lower-level tools and abstraction techniques that interface both vertically and horizontally to provide system-level optimization between disparate-technology point tools. Many of these tools, in fact, exist outside of Chatoyant. However, by providing a common framework and common software interfaces to these tools, we support the designers in their exploration of a multitechnology design space.

For example, as indicated in Fig. 2 with bold arrows, electrical simulations that give results on the power dissipation of OE components can be tied through thermal analysis to packaging and alignment models. That analysis can give positional variance information to the Gaussian beam propagation models to characterize noise, insertion loss, and cross talk.

In Section 3 we discuss our technique for providing system-level models and give several examples of signal and component models. This is followed by a discussion of how Chatoyant incorporates these mod-

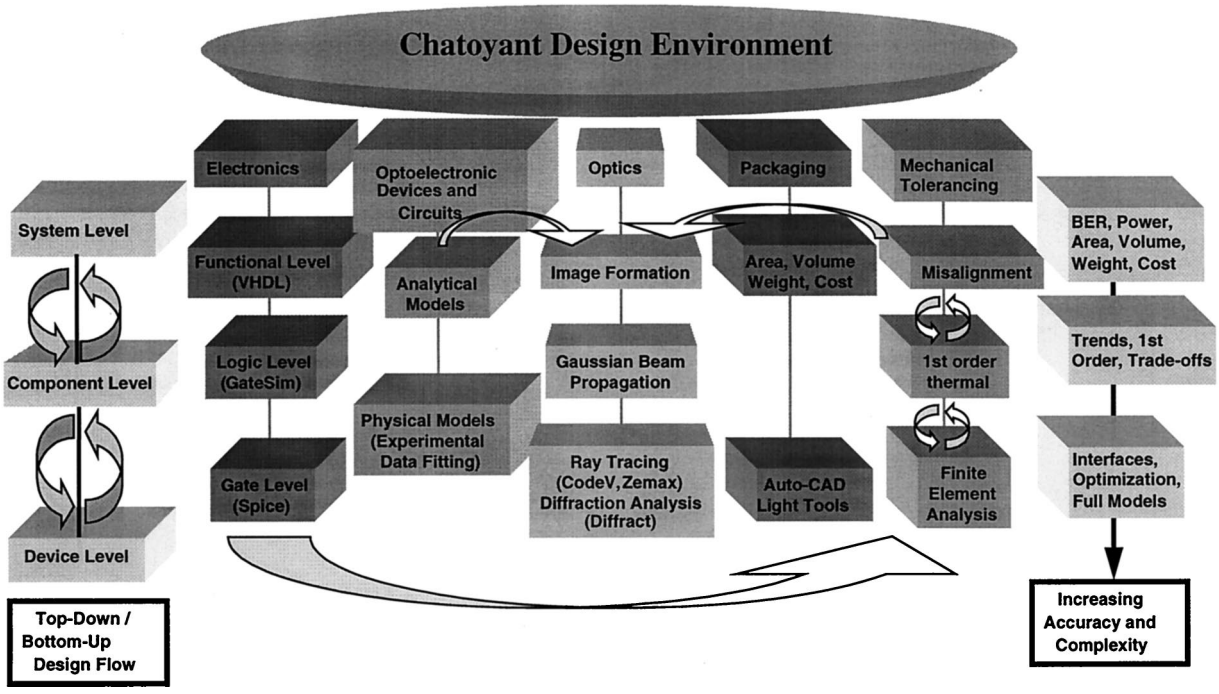

Fig. 2. OE system design issues.

els. Finally, we show the use of Chatoyant for performing system-level trade-off analyses across multiple domains.

3. System-Level Modeling

A system-level model can be defined in terms of its models of modules, the signals that pass between them, and the dynamics of the system behavior in terms of the ways in which the modules affect the signals. For OE systems our signals are represented as electronic waveforms, mechanical movements, and modulated carriers, i.e., beams of light. For light the characteristics of the optical carrier are as important to model as the signal itself. It is also important that we have the ability to support multiple representations at different levels of detail. This provides for the choice of accuracy versus speed of computation within the analysis framework. Therefore we need to have a flexible model for the propagation of both electronic and optical signals. Using the characteristics of the optical and the electronic signals, which carry information between the components, we have defined models for the system component modules in terms of the ways they transform the characteristic parameters of these signals. Finally, our model of the dynamic system behavior is based on a time-domain analysis of the propagation of the signals through the components.

A. Models of Signals

Our methodology for modeling OE signals has been defined to meet our needs for system-level simulation. These can be summarized as representing digital data throughout the system for functional simulation as well as analog waveforms for accurate modeling of speed, noise, and cross talk. Additionally, we must allow the user to control the trade-off between speed of simulation and accuracy of simulation at run time. Finally, we must provide compatibility with other existing simulation and analysis tools, both digital and analog. Therefore we model electronic signals as piecewise linear voltage amplitudes with characteristic source impedance. We can vary the speed and the accuracy of our electronic simulations by simply varying the sampling rate for the piecewise linear signals. Of course, for optical signals there are additional concerns.

There is a range of abstractions that can be used for modeling optical signal propagation. For system-level design and analysis, we have chosen to support geometric optics for the most basic analysis and Gaussian beam models for more accurate simulations.[18] We capture the intensity, position, angle, and wavelength for ideal optical rays, as well as the depth of focus and spot size for Gaussian optical beams.

However, one problem with the Gaussian beam model is that the approximation fails in several instances. In particular, it is inaccurate when sources do not generate a Gaussian intensity wave front, when the direction of propagation of the light does not meet the paraxial criteria, and when diffractive effects must be considered.

Most important to us are the cases in which the beams are clipped by the optical components through which they pass. In those cases the classical equations for intensity and beam waist break down. These cases can occur for systems with arrays of microlenses, or lenslets, in which logical or physical constraints on the system cause splitting or clipping

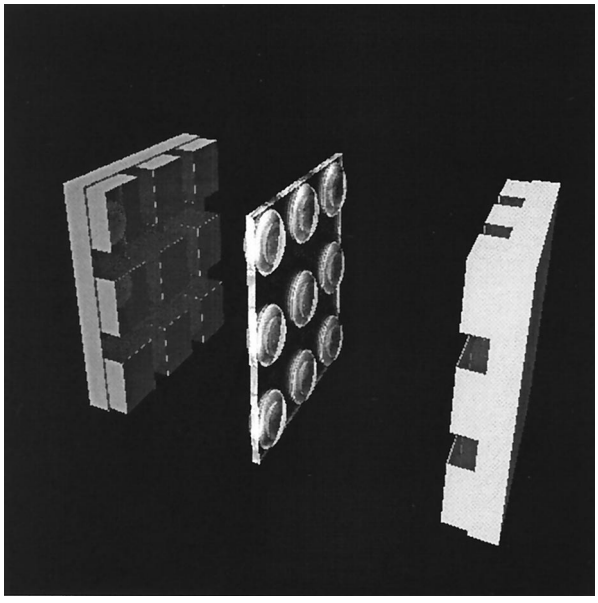

Fig. 3. Lenslet array.

of the Gaussian beams. Figure 3 shows a picture of a 3×3 lenslet system drawn by Chatoyant, which uses an interface to Sced[19] and is rendered with Persistence Of Vision.[20] It is for these kinds of systems in which the sizes of the lenses themselves are of the order of the dimensions of the Gaussian beams (5–40 μm) that we must concern ourselves with clipping as well as misalignment and tolerancing.

We model a lenslet as a lens bounded by a small aperture.[21] The power lost in a Gaussian beam that is clipped by an aperture is $P_{\text{new}} = P[1 - \exp(-2k^2)]$, where $k = D_{\text{apt}}/(2W_{\text{apt}})$ is the ratio of the diameter of the aperture to the beam's diameter at the aperture. For $k > 2.12$ the clipping is less than 0.1% and diffractive effects are negligible. For severe clipping ($k \leq 1$) the beam-intensity profile is no longer Gaussian and the Gaussian approximation breaks down completely. For moderate clipping ($1 < k \leq 2.12$) the beams are weakly diffracted and a Gaussian approximation can be used with a slight modification.[22] In this moderate range the power loss varies from 13% to 0.1%. However, the loss in power is not the most significant change of a clipped beam. The diffractive effects cause the beam to distort its shape. This distortion is modeled by propagation of a new effective Gaussian beam with a new effective beam waist:

$$W_{0\text{eff}} = W_0\left[1 - \exp(-x^2/2)\cos\left(\frac{px^2}{4\pi}\right)\right],$$

where $x = k\sqrt{2}$ and $p = 2\pi(z/z_0)$. In this equation, z is the propagation distance and z_0 is the Rayleigh range. This effective beam replaces the original Gaussian beam, and normal thin-lens propagation models are used to model the clipped beam.[23]

Although the clipping at the aperture will decrease the total power, it is interesting to note that the co-

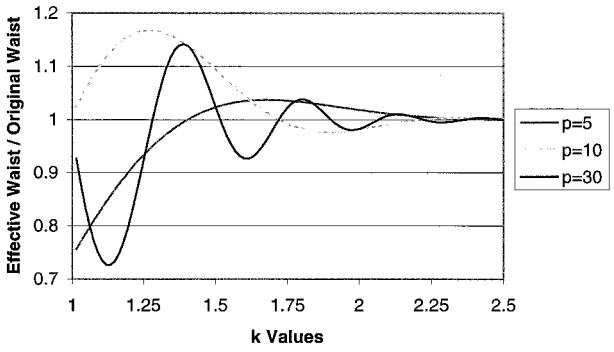

Fig. 4. Diffractive effects on a clipped Gaussian beam.

sine term can be either positive or negative, allowing the effective waist to become either larger or smaller than the initial waist. This diffractive effect on the waist is shown in Fig. 4, in which the effective waist is a function of p, seen above, and the clipping ratio k.

To test this approximation technique, we compared the results of Chatoyant with another optical CAD tool, LIGHTPIPES.[24] LIGHTPIPES uses Fourier analysis for the propagation of light through space and optical components. The optical system used in this comparison is a $2f$ system with both the source and the detector arrays placed 100 μm away from a lenslet array ($f = 50$ μm). The source beams are 850-nm, 10-μm spots, which give a p value of 1.7. This system is the same as that shown in Fig. 3. The lenslet's diameter is varied to produce different amounts of clipping. Figure 5 shows a graphical comparison between Chatoyant and LIGHTPIPES for the power lost because of Gaussian beam clipping within the moderate clipping range ($1 < k \leq 2.12$). Our results show that the worst-case difference between the two CAD tools is approximately 0.85%, with an average difference of approximately 0.29%. Therefore for

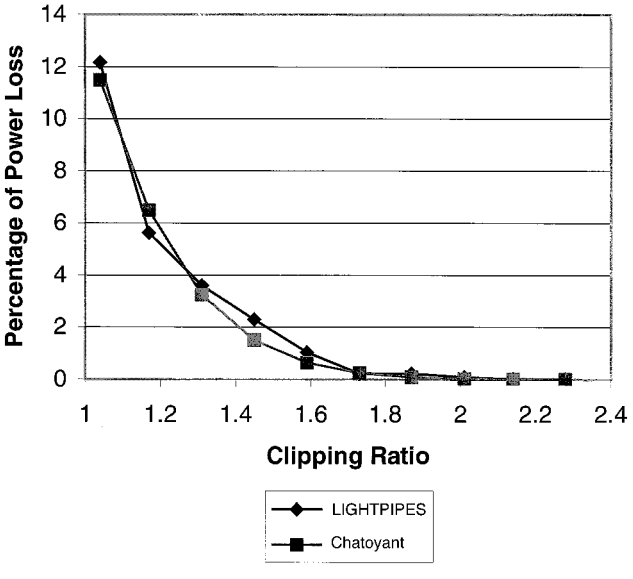

Fig. 5. Power-loss comparison between Chatoyant and LIGHTPIPES.

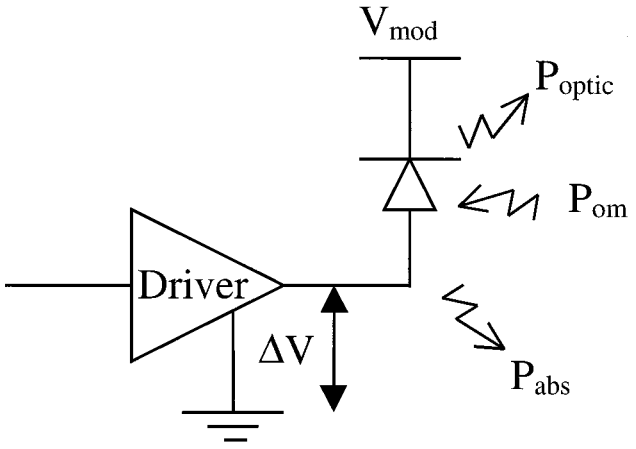

Fig. 6. Modulator schematic.

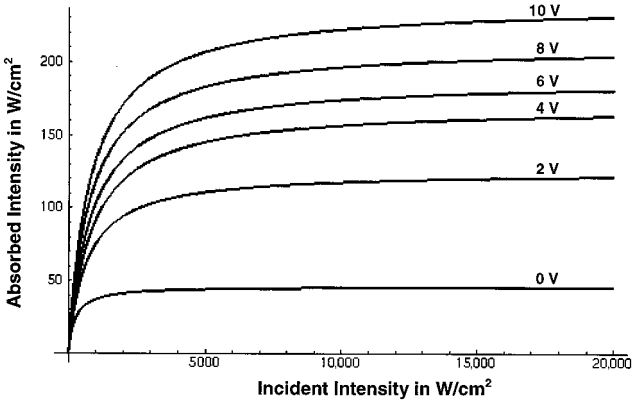

Fig. 7. Absorbed versus incident optical intensity (in watts per square centimeter).

the case of paraxial Gaussian beam propagation our corrections for moderate clipping compare favorably with detailed, but slower, Fourier modeling techniques.

B. Modeling Components

Similar to our signal models, component or device models have also been developed at varying levels of abstraction. In general, we have developed three techniques for capturing component models: analytical models, empirical models, and lumped-parameter models. By analytical models we mean those models that are based directly on equations that model the physical processes of the device. These equations can be simplifications of the true behavior of the device or can capture as much detail as desired. In any case they are distinct from the empirical models that are based on measured data represented either as continuous curves or simply tabular data. Our third modeling technique takes advantage of the support for multiple abstractions within the Chatoyant framework. Lumped-parameter models are those derived from the execution of lower-level simulation and analysis tools. Although these models are also approximations, they are accurate at the level of abstraction required for system-level design and analysis. We give examples of each of these modeling techniques below for a few of the components we have modeled to date.

1. Empirical Models for Multiple-Quantum-Well Modulators

As an example of empirical modeling, we present our model for multiple-quantum-well (MQW) modulators. Figure 6 shows both the driver electronics and a MQW modulator reflecting a portion of the incident light P_{om} as modulated optical power P_{optic}. Both reflective and transmissive modulators are possible. In either case the key parameter is the amount of optical power that is absorbed by the modulator as a function of the controlling voltage.

The relation of the modulation voltage to the absorbed optical power is modeled with a Lorentzian line shape:

$$P_{\text{abs}}(V) = \frac{P_{\text{om}} k(V)}{1 + \dfrac{P_{\text{om}}}{A I_s(V)}},$$

and the reflected optical power is $P_{\text{optic}} = P_{\text{om}} - P_{\text{abs}}$. The function $k(V)$ is the absorption slope of the MQW, $I_s(V)$ is the saturation intensity of the MQW, and A is the area of the modulator. The terms $k(V)$ and $I_s(V)$ are interpolated from empirical measurements of MQW modulators.[25] Figure 7 shows this incident-intensity–to–absorption-intensity relation for typical values of modulation voltage.

2. Analytical Models for Vertical-Cavity Surface-Emitting Lasers

An example of a simple analytical model is the technique we use for vertical-cavity surface-emitting lasers (VCSEL's). Figure 8 shows a schematic of the VCSEL and the drive circuitry. The term R_s is the series resistance, and C is the total parasitic capacitance associated with the VCSEL and the assembly

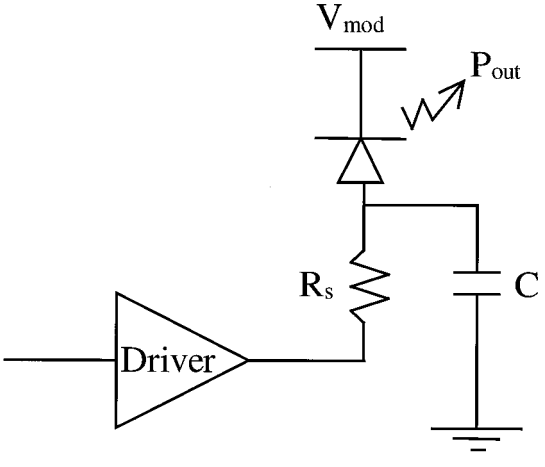

Fig. 8. VCSEL schematic.

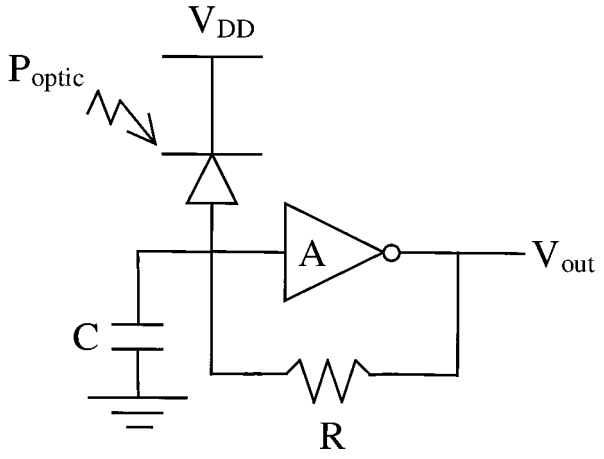

Fig. 9. Receiver schematic.

technology that connects the VCSEL array to a VLSI chip.

Modeling VCSEL's analytically, we concentrate on the relation between the input electrical power and the output optical power:

$$P_{\text{out}} = \frac{\eta_{\text{LI}}/V_{\text{th}}}{(1 - \eta_{\text{LI}}/V_{\text{th}})}(P_{\text{in}} - I_{\text{th}}V_{\text{th}}),$$

where I_{th} is the laser threshold current, V_{th} is the laser threshold voltage, η_{LI} is the laser slope efficiency, and P_{in} is the input electrical power.

One of the main concerns of VCSEL researchers is the VCSEL's threshold power.[26] For the laser to emit, the input power must overcome the threshold power. In general, this power threshold is much larger than that of the MQW. The VCSEL driver must be larger (up to 20 times larger) than the MQW driver to overcome the power threshold and drive enough current to allow the laser to emit. Therefore, as discussed below, accurate modeling of the driver electronics becomes important.

3. Lumped-Parameter Models for Receivers

A generic single-ended receiver is shown in Fig. 9. The two primary components are a photodiode and a transimpedance amplifier. This circuit was simulated with SPICE, and the parameters were extracted and used to define the s-domain transfer function for system-level simulation. We use the transfer function of a transimpedance amplifier with a feedback resistance, where R is the total resistance, C is the total capacitance, and A is the gain of the amplifier:

$$V_{\text{out}}(s) = \frac{R}{1 + \left(\frac{RC}{A}\right)s} P_{\text{optic}}(s).$$

When the inverse Laplace transform is performed on the transfer function, the time-domain relation of the input optical power to the output voltage for the single-stage transimpedance amplifier can be determined. The voltage output function is dependent on both the signal input and the state of the transimpedance amplifier. When a piecewise linear waveform is used, the final equation in the time domain is

$$V_{\text{out}}(t + \Delta t) = XR\left\{\frac{RC}{A}[\exp(-y) - 1] + \Delta t\right\} + P_{\text{in}}(t)R[1 - \exp(-y)] + V_{\text{out}}(t)\exp(-y),$$

where $X = [P_{\text{in}}(t + \Delta t) - P_{\text{in}}(t)]/(\Delta t)$ and $y = \Delta t[A/(RC)]$. We use similar methods to approximate the dynamic response of each of the OE modules in the system.

4. Driver Models

For some components our modeling technique is a mixture of analytical and lumped-parameter models. We develop an analytical model and use lower-level tools to tune our models to match the performance of these more accurate, but slower, analysis tools. This is the case for our models of driver electronics.

As mentioned above, modeling the dynamic response of the electronic drivers for both MQW and VCSEL sources is crucial for Chatoyant to model the OE interface correctly. These models enable the user to make fast evaluations of mixed-technology designs without using a more accurate tool, e.g., SPICE.

Many drivers in OE circuits are created when complementary metal-oxide semiconductor (CMOS) inverters are placed together to create a multistage driver. Therefore we concentrate our efforts on modeling a simplified model for a CMOS inverter. However, for reasonable accuracy this model depends on the dynamic values for the gain and the input and the output impedances throughout the entire range of the input signal. Therefore we find that a small-signal model analysis is impractical because of the large-signal nature of the input signal. These electronic driver models also include the effects of both internal and parasitic RC delays.

The starting points for our model are the ideal, first-order equations of Shockley.[27] Under ideal conditions these equations describe the behavior of an n-type metal-oxide semiconductor (NMOS) transistor in its typical three regions: cutoff, saturation, and nonsaturation (both linear and triode).

In a CMOS inverter two transistors switch between these three states according to the excitatory input. With classical small-signal methods this transition of states is modeled as five possible states in which the transistor pair can be found.[28] The simplification is due to the assumption that the inverter does not have any electrical load in its output. Consequently, the output current is defined for the matching point of operations of both transistors. Therefore dynamic analysis by use of this model is possible only as a small-signal model.

However, when we need to perform large-signal analysis to account for amplifier saturation effects (e.g., overdriving the input produces square waves),

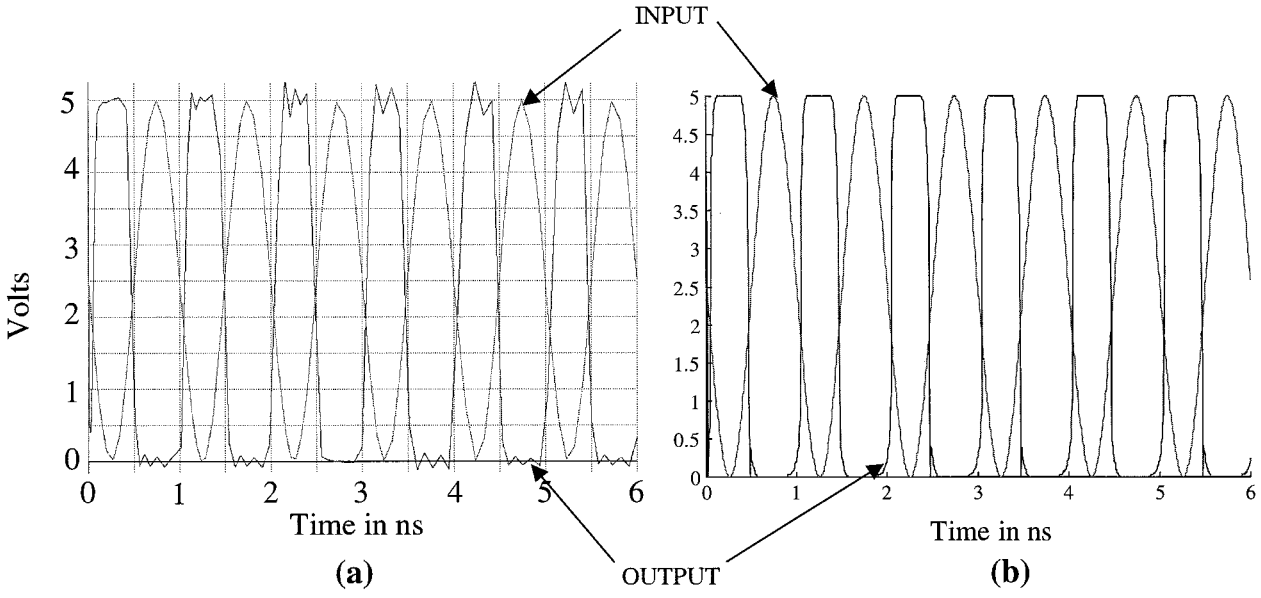

Fig. 10. CMOS inverter response (C_{out} = 1 fF, 100 MHz) with (a) SPICE and (b) Chatoyant.

we must model the inverter with fixed power supplies and load conditions. Under these conditions the classical method for determining the small-signal parameters, the amplifier transconductance g_m, and the output conductance g_{ds} is no longer valid. Both terms change dynamically throughout the different ranges of operation and need to be calculated continuously. Therefore output values for both voltage and current at time $t + \Delta t$ can be obtained with these dynamic parameters and the above output values at time t. Here the effect of the external load is considered as a temporary current sink or source.

In our model the inverter's state of operation is used to determine the dynamic parameters of only g_m and g_{ds}. These parameters are derived from the Shockley equations, considering the appropriate partial derivatives. The final expressions for the CMOS inverter model are

$$V_{out}(t + \Delta t) = V_{out}(t) + \frac{g_m}{g_{ds}}\{\exp[(g_{ds}/c)\Delta t] - 1\}\Delta V_{in} + \frac{I(t)}{g_{ds}}\{\exp[(g_{ds}/c)\Delta t] - 1\},$$

$$I_{out}(t + \Delta t) = I_{out}(t) + g_m \Delta V_{in} + g_{ds}\Delta V_{out}.$$

Figure 10(a) shows a SPICE simulation and Fig. 10(b) shows our simulation for an inverter input and response with a load of 1 fF operating at a frequency of 100 MHz. Figures 11(a) and 11(b) again show SPICE and Chatoyant simulations, respectively, for a 100-MHz system with a comparatively large load capacitance of 1 pF.

Comparing the simulations in Fig. 10, we see that the SPICE and the Chatoyant results are similar. Both show the inverter operation working correctly, with the output saturating at the power supply. However, there are slight differences. The main differences observed are caused by the influence of the input signal over the output circuit through C_{gd}, the gate-drain capacitance. We have not yet included this capacitance in our models.

In Fig. 11 we again see that the results are very close between SPICE and Chatoyant. In this simulation the load capacitance is too large to be charged completely by the inverter. Therefore the output swing does not complete its transition before the input value changes. Also, both simulations show the result of the fact that the p transistor (pull-up) has a lower value of β than the n transistor, causing the output of the inverter in the steady state to be centered at approximately 1 V instead of at $V_{dd}/2$.

4. System-Level Simulations with Chatoyant

In Chatoyant system simulation is based on the Ptolemy environment developed at the University of California at Berkeley.[29] Ptolemy is an object-oriented platform designed to support complex and heterogeneous simulations. In Section 3 we noted that the key elements of a system-level simulation were the representation of component models, communications, and interaction. In Ptolemy a component model is implemented as a programming object called a *star*. Written in the style of C++, each star defines the behavior of a component at a specific level of abstraction chosen by the user. Like C++ object classes, each star also defines a set of signals for communication with other stars in the system model. The specific interactions among the stars are determined by a combination of this communication model and a specific Ptolemy *domain* that defines the scheduling discipline used during simulation computations. A number of built-in stars also exist within Ptolemy for stimulus generation and graphic display of results. In addition, the system provides a graphics–user interface in which users can construct

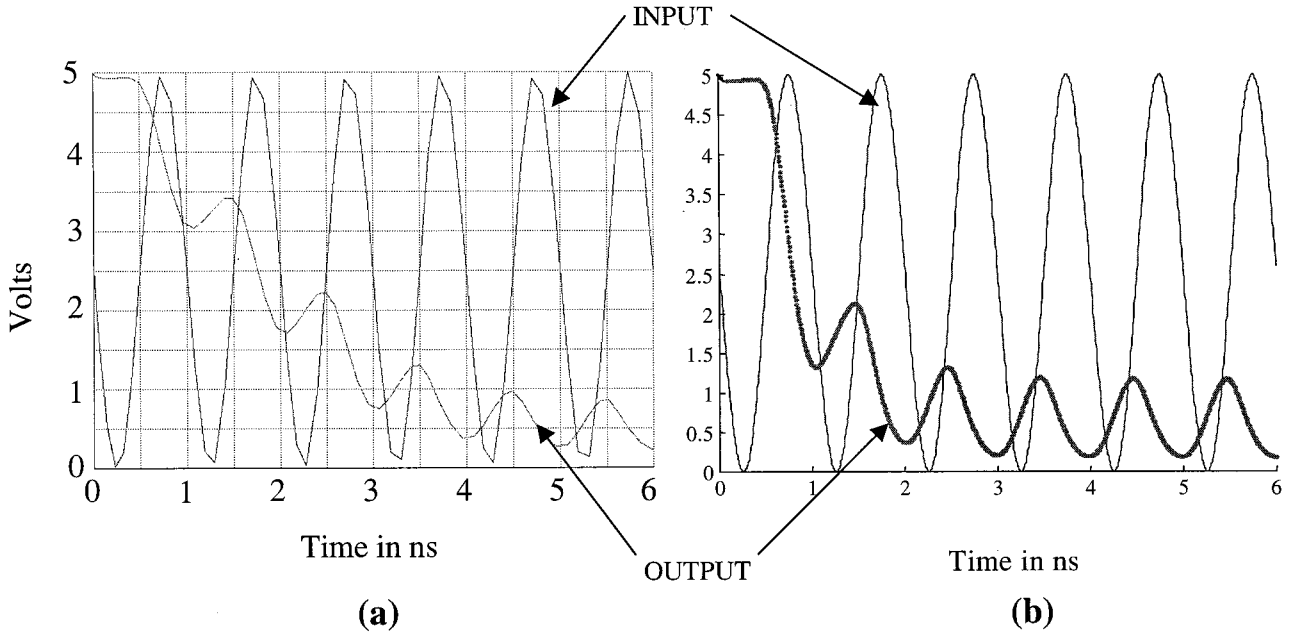

Fig. 11. CMOS inverter response (C_{out} = 1 pF, 100 MHz) with (a) SPICE and (b) Chatoyant.

systems by graphically interconnecting icons that represent the particular modeled devices.

Our models for signals are implemented as a message class in the object-oriented framework of Ptolemy. This means that the characteristics of the signal are an encapsulated data type that can be changed as needed. Currently we capture the voltage and the characteristic source impedance of electronic signals; the intensity, position, angle, and wavelength for optical signals; and the depth of focus, spot size, and profile for Gaussian optical beams.

Figure 12 shows a simple 4*f* system as modeled in Chatoyant. Each icon, or star, represents a basic OE component or input–output function. The ModArray input star allows us to simulate arrays of arbitrary data patterns that are modulated onto an array of laser light beams. The XMgraph output star displays either the voltage or the optical intensity of a single pixel during simulation. For the simulations the ModArray interpolates a sequence of arrays of bit patterns (read from a file) into piecewise linear voltage waveforms that drive the MQW modulator models described in Subsection 3.B.1. The resulting optical intensity waveform is passed through the lens models obtained from the Gaussian propagation equations. The PowerGrid star is used to observe power in an x–y cross section of the optical signals. Additionally, it can show the placement and the power received by an array of ideal detectors. On the other hand, the DetectArray star models the dynamics of the receiver models first by integration of the intensity from each Gaussian beam over the area of each detector and then by transformation of the optical power waveforms into voltages, as shown above.

A. Beam Shape, Position, and Power

Figure 13 shows how Chatoyant simulates beam shape, position, and detected power for this simple nine-channel link. Figure 13(a) graphically illustrates the modulation voltages for a 3 × 3, 20-μm spot-size, 40-μm spacing, MQW modulator array. The black squares represent 0-V and the white

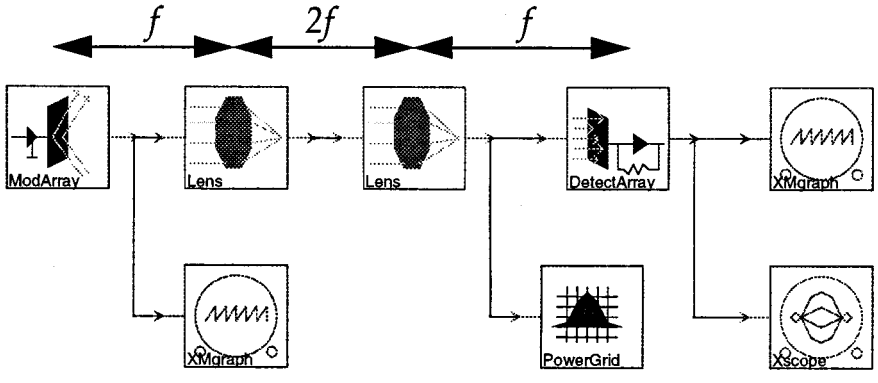

Fig. 12. Description of a 4*f* system in Chatoyant.

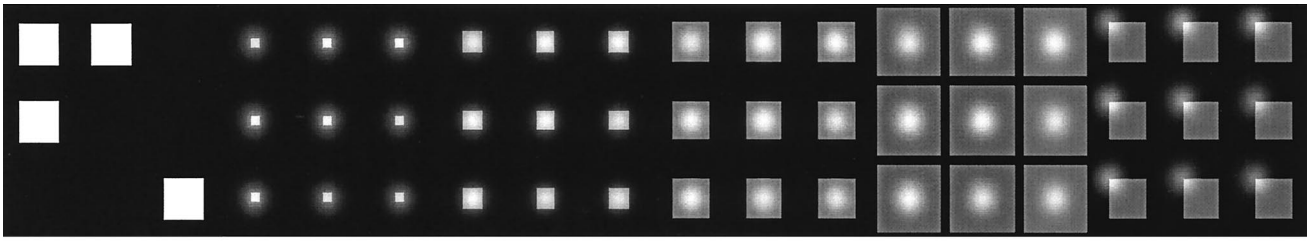

(a) (b) (c) (d) (e) (f)

20-μm Modulators			5-μm Detectors			10-μm Detectors			20-μm Detectors			35-μm Detectors			20-μm Offset		
771	906	906	113	133	133	360	422	422	703	826	826	771	905	905	193	227	227
906	906	771	133	133	113	422	422	360	826	826	703	905	905	771	227	227	193
906	771	771	133	113	113	422	360	360	826	703	703	905	771	771	227	193	193

Fig. 13. Static simulations: power (in microwatts) detected at different size detectors.

squares 10-V modulation. The source power comes from nine 1-mW spots generated by an 850-nm laser. The table of Fig. 13(a), found below the image, shows the optical power reflected into the system by each of the modulators. The table shows the lack of modulation depth (a contrast ratio of 1.17, or approximately 1.4 dB) typical of MQW modulators. Figures 13(b)–13(f) show graphically, and their corresponding tables show numerically, the power (in microwatts) detected by an array of receivers after the light has passed through a 4*f* imaging lens system. In all the figures one can see the Gaussian intensity profile of the 20-μm beams.

For these figures the Gaussian intensity profile is generated by the individual integration of the power at each square of a user-defined grid laid down on top of the detector array. This allows Chatoyant to show the variations in power across each detector, at the expense of computation time T, where $T = k(\text{number of channels})(\text{number of grid squares}) + c$, where $k = 1.03 \times 10^{-5}$ s and $c = 0.09$ s. Each of the images in Fig. 13 took approximately 1.0 s to compute on a P6-180 running Linux. For most simulations, for which we are concerned with only the total power captured on each detector, we do a single integration for each detector, so $T = k(\text{number of channels})(\text{number of detectors}) + c$.

Returning to Fig. 13, we note that the image is inverted in intensity because of the inverting properties of the modulators and is inverted spatially because of the 4*f* lens system. Figure 13(b) shows an array of modulated beams imaged on an array of detectors in which the photodiode of each detector is 5 μm × 5 μm. Figures 13(c), 13(d), and 13(e) show 10 μm × 10 μm, 20 μm × 20 μm, and 35 μm × 35 μm detectors, respectively. Note that, for the 35-μm detectors, almost all the power from the modulators is recovered. Figure 13(f) shows the power detected by the 20 μm × 20 μm detector array for the case in which the second lens of the 4*f* system has a small (10-μm) misalignment in both the x and the y positions. This simple example shows how Chatoyant can be used to estimate the required mechanical tolerances of OE systems.

Another feature of our system is the ability to show the y–z cross section of a Gaussian beam as it propagates through a system. This is useful because it allows the user to analyze the waist of the beam at any point in the system and determine where the focus of a complex lens system will be. Figure 14(a) shows a Chatoyant representation of a system that uses the GaussCross star. Again, the system is a 4*f* system; however, now a 3 × 3 VCSEL array with a 20-μm spot size and 40-μm spacing is used to source the system. For the purposes of illustration, lenslets with a diameter of 36 μm are used in this system; however, because of clipping, they are too small to provide perfect imaging. Figure 14(b) shows the Gaussian cross section between the components throughout the system. Note that, at the lenses, the waist diameter is approximately 33.5 μm, which gives a k clipping ratio of 1.07. The beams at these interfaces lose approximately 10.1% of their power. Also note that the diffractive clipping effects also alter the final size of the Gaussian waist at the detectors. The initial 20-μm spot is distorted and is detected as an approximately 24-μm spot.

B. Dynamic Response, Noise, and Bit-Error Rate

For the same MQW nine-channel link system shown in Fig. 12, Chatoyant can also perform dynamic simulations of data streams through the link. Figure 15 shows one piecewise linear signal at the two XMgraph monitor points: the output of one of the modulators, showing intensity (in watts per square meter), and the output of one of the detectors (in volts). The Xscope output star shows a voltage eye diagram for this random sequence of bits. Figure 15(a) shows operation at 100 MHz, and Fig. 15(b) shows bit rates of 300 MHz. Here the detectors were each 20 μm and the receiver model parameters were $A = 1$, $R = 4$ kΩ, and $C = 250$ fF. As explained below, noise was added to the system for more realistic dynamic modeling. In this example the inci-

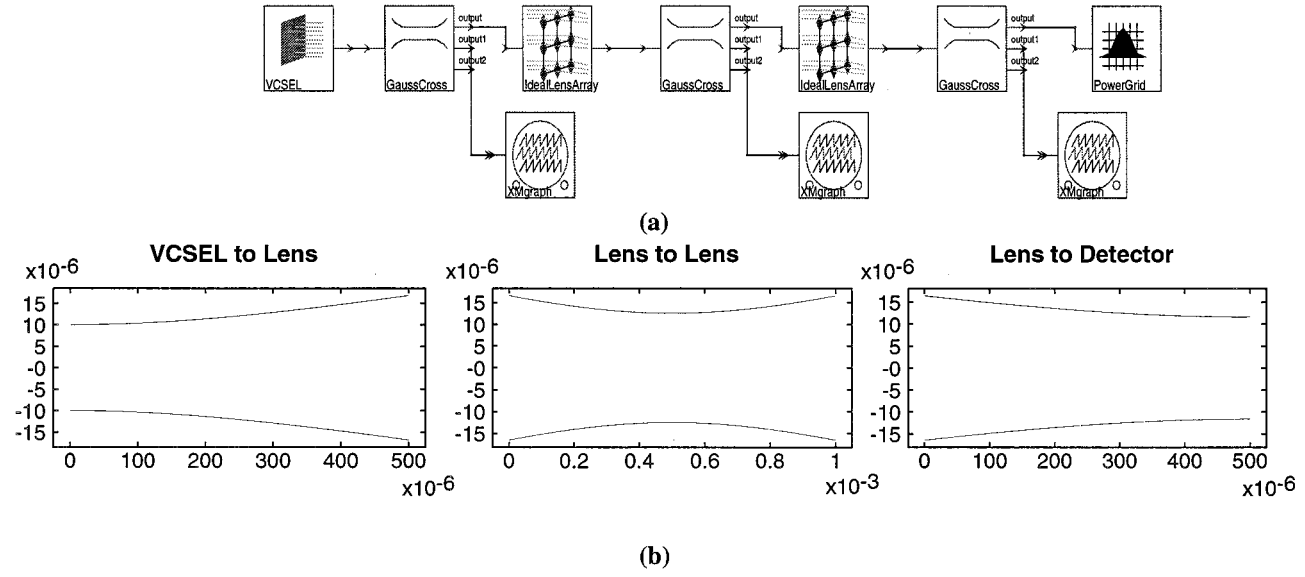

Fig. 14. (a) System in Chatoyant. (b) Cross section of a Gaussian beam.

dent laser power that is modulated by the MQW was lowered to 10 μW. We show the degradation of the noise margin that occurs because of the lack of dynamic response of these relatively large detectors, from 100 to 300 MHz. The noise margin is defined as the ratio V_1/V_2, in terms of the minimum excursion V_1 and the maximum excursion V_2 of the received signal. We can see that the noise margin drops from 96% to 52% between the two systems.

We model a noisy signal by using classical Gaussian noise methods. This requires determining the noiseless signal, which has no variance, and adding to it a noisy random signal, which has a mean understood to be zero. Currently, in our system noise is accounted for in only the photoreceiver and the input into the transimpedance amplifier. The detector's noise sources that we model include the thermal, or Johnson, noise, the shot, or quantum, noise, and the thermal noise that is found in the conducting channel of the amplifier drive transistors. All noise components are modeled with Gaussian noise distributions.[30] An important characteristic of Gaussian noise distributions is that the distributions are additive. Therefore each noise source determines its own contribution to the total noise, and then all the noise sources are added together to find the total Gaussian noise variance of the system.[31] From the total Gaussian variance a random-noise component is calculated that is added to the photocurrent as it is produced by the p-i-n detector diode. This noisy photocurrent is then amplified and converted into voltage through the transimpedance amplifier.

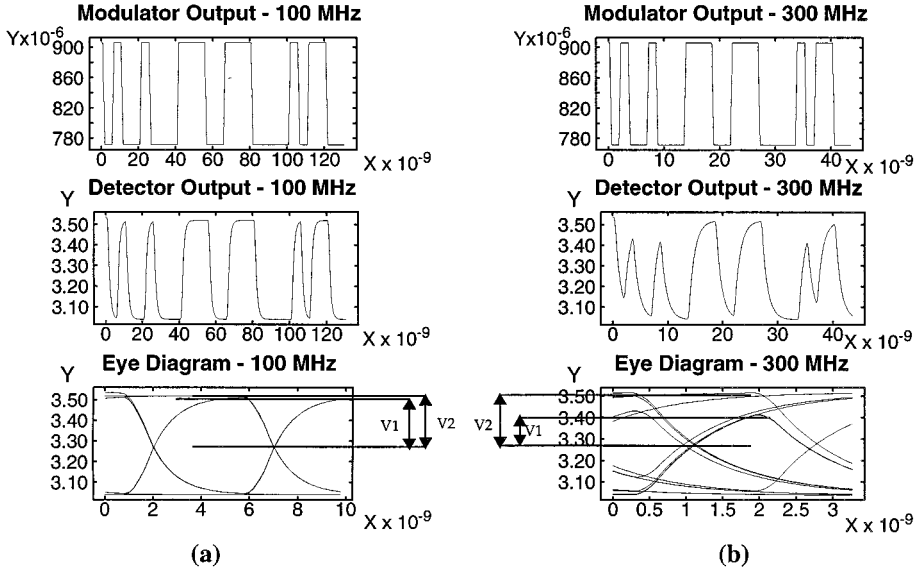

Fig. 15. Modulator and detector single-pixel dynamic simulations.

From this noise modeling the system automatically calculates the BER of the data stream propagating from the source to the detector, as described below.

1. *Bit-Error-Rate Simulation*

Chatoyant can also be used to predict the BER of FS OE systems. We have concentrated our efforts on modeling the relation of sampling times and decision threshold levels to mechanical and thermal tolerances.

The BER can be determined by simulation in many different ways, such as with Monte Carlo simulations, importance sampling, the extreme-value technique, and the tail-extrapolation technique.[32] We use a quasi-analytical approach in our determination of the BER. Similar to determining a noisy signal, as seen in Section 3, the quasi-analytical approach separates the BER determination into two parts. The first part determines the noiseless signal, and the second part analytically determines the noise distributions. With this method the following equation gives the BER in a series of detected bits[33]:

$$\mathrm{BER} = \frac{1}{2N}\sum_{i=1}^{N}\left[\operatorname{erfc}\left(\frac{V_i - V_{\mathrm{th}}}{\sigma\sqrt{2}}\right)u(V_i - V_{\mathrm{th}}) + \operatorname{erfc}\left(\frac{V_{\mathrm{th}} - V_i}{\sigma\sqrt{2}}\right)u(V_{\mathrm{th}} - V_i)\right],$$

where N is the total number of bits in the simulated process, V_i is the received noiseless signal value for the transmitted bit at the sample time, V_{th} is the threshold level, and σ is the standard deviation value of the noise. The step function u is used in the equation to determine whether V_i is greater or less than V_{th}.

The BER is dependent on the sampling time and the decision threshold. The sampling time is defined as the instant that the received data are sampled to determine their logic level. For obtaining the lowest BER the sampling time needs to be at the most open portion of the eye diagram. The significance of the sample time is shown graphically in Fig. 16(a). Here the BER of a 300-MHz, 4f system with a received photocurrent level between 4 and 5 μA is determined at different sampling points. The noise variance σ^2 for this system is approximately 9.7×10^{-16} A^2. The ideal sampling point is set in the middle of the graph (at 0 ps), and the BER of this system, with sampling times offset from the ideal sampling time, is calculated. This ideal sampling point refers to approximately 2.1 ns on the eye diagram found in Fig. 15(b). As seen in the graph in Fig. 16(a), a BER of approximately 10^{-8} can be achieved in a sampling window of approximately 120 ps. Note that, if the sampling time is not exact, the BER can increase by 3.5 orders of magnitude with only a 300-ps offset from the ideal sampling time.

The next example shows how the received photocurrent affects the BER. For a 250-MHz system the received photocurrent is varied and the BER is plotted with respect to the received photocurrent.

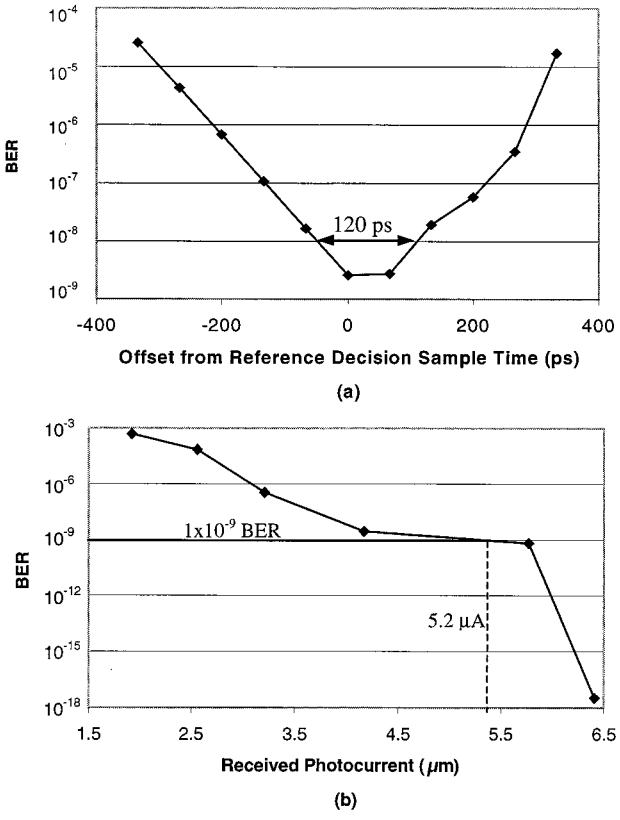

Fig. 16. BER simulations: (a) sampling time and (b) photocurrent received.

Figure 16(b) shows this BER–photocurrent relation. The photocurrents that were measured and plotted were approximately 1.9, 2.6, 3.2, 4.7, 5.8, and 6.4 μA. Note that, for obtaining a BER lower than 10^{-9}, a received photocurrent of approximately 5.2 μA is required. The BER drops substantially after the received current is greater than approximately 5.8 μA. Krishnamoorthy *et al.*[34] have published results on this photocurrent-to-BER relation for a similar receiver circuit. They also examined a 250-Mbit/s system and found that a minimum photocurrent of 3.5 μA is needed to achieve a BER of less than 10^{-9}. Their system used a three-stage amplifier, which could account for this small difference.

2. *Insertion Loss and Cross Talk*

In this example we modeled a 4f (f = 2 mm) system with a single 850-nm, 20-μm spot-size source and a source–receiver spacing of 25 μm. Different sized detectors (5, 10, 20, and 25 μm) were used to detect the beams. Cross talk was measured by a comparison of the amount of power detected on an adjacent detector with that of the power detected on the desired detector. Because cross talk can affect many detectors, the worst-case received power on any single detector was used. Insertion loss is the ratio of the received to the transmitted power. We simulated lateral and longitudinal displacements in the detectors and plotted both the insertion loss and the cross talk in the system.

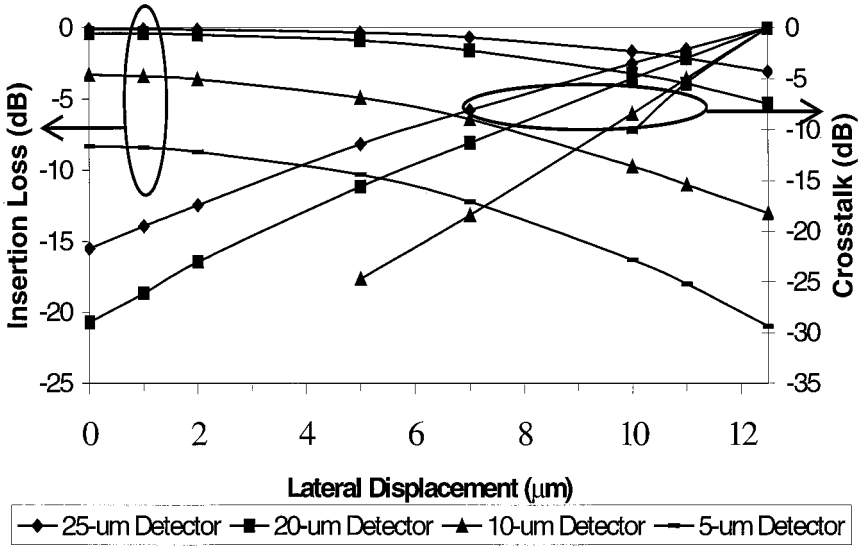

Fig. 17. Insertion loss and cross talk versus the lateral displacement.

The graph in Fig. 17 shows the insertion loss, graphed on the left-hand y axis, and the cross talk, graphed on the right-hand y axis, for a system experiencing lateral displacement, as shown on the x axis. The cross talk will always be 0 dB at a distance of half the detector spacing, in this case at 12.5 μm, because of the beam's being directly between two detectors and each detector's receiving an equal amount of power.

Figure 18 again shows the insertion loss and the cross talk, in this case for longitudinal displacement from the ideal focusing point of the system. Note that the system was much more sensitive to lateral displacement than to longitudinal displacement. For example, the 20-μm detector has the same insertion loss (approximately −2.3 dB) for a lateral displacement of 8.5 μm as it does with a longitudinal displacement of 500 μm. At these same displacements, the cross talk is much larger at the lateral displacement (−7 dB) than at the longitudinal displacement (−13 dB).

C. Mixed-Technology System Trade-Offs

Figure 19 shows a FS OE system used for intrachip neighborhood interconnections. When a mirror facet is fixed at a specific angle, interconnections can be made from one node to another node on the chip. We use this system to show how we can use Chatoyant to perform trade-offs among the detector size, the mechanical tolerance on the position of the mirror, the BER, and the operating speed of the system.

In this system the source beam propagates through a lens, reflects off of a mirror, propagates through another lens, and then is received by a photodetector.

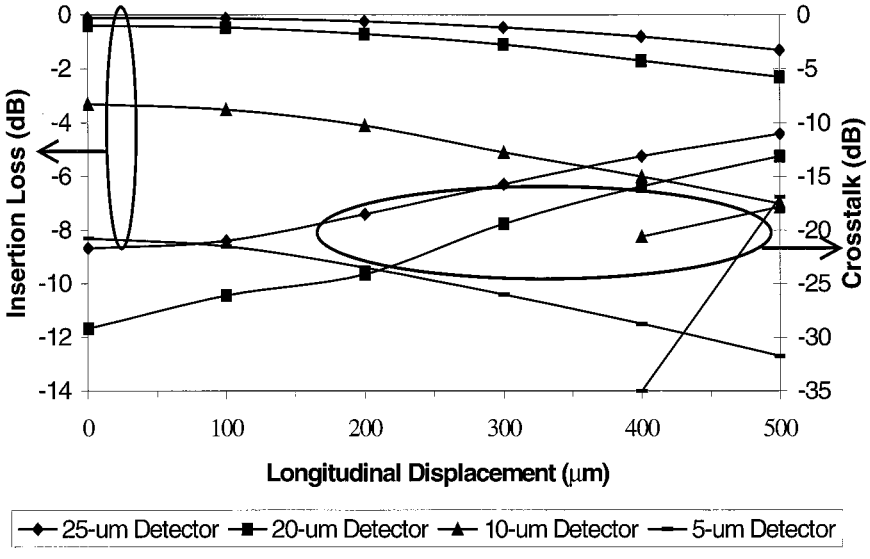

Fig. 18. Insertion loss and cross talk versus the longitudinal displacement.

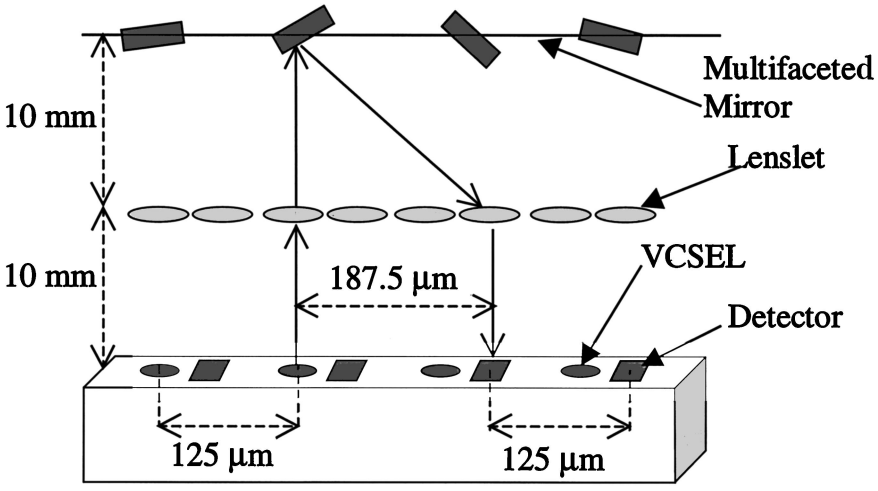

Fig. 19. On-chip neighbor processing node interconnect.

The source beams are 10-μm spots placed in a 4×1 array and spaced by 125 μm. The distance between each of the components on the optical path is 10 mm, with the lenses also having a focal length of 10 mm. Thus this system is just an ideal $4f$ system with a mirror placed between the two lenses.

This system is operated within the range from 100 to 500 MHz, and the BER is calculated for the received bit pattern with different-sized detectors. The detectors have side lengths of 5, 10, 15, and 20 μm. Each of these detectors has a lumped capacitance relative to the detector size and a fixed parasitic capacitance, giving total capacitances of 100, 125, 200, and 325 fF, respectively. The advantage of using the larger detectors is the amount of power that the detectors can receive; however, the higher capacitances degrade the system's dynamic performance.

A graph of the speed versus the BER of the system is shown in Fig. 20(a). This graph shows the simulation for an ideal mirror position, meaning the angle of the mirror is exact and there is no offset or misalignment. Note that, at slower speeds (<200 MHz), all the detectors have a BER of less than 10^{-12}. Above approximately 250 MHz, the largest detector (20 μm) has the worst system BER. The large capacitance associated with the 20-μm detector affects both the calculated noise variance and the received signal amplitude. With the high noise variance and deteriorating noise margin, the BER of the 20-μm detector increases quickly. The BER for the 15-μm detector is always smaller throughout the range of frequency compared with that of the 20-μm detector; however, the 10-μm detector appears to be the best detector for this system. This detector has a good mix of size and speed, meaning that it is big enough to capture most of the transmitted signal but small enough to have a good dynamic response. In contrast, the 5-μm detector has the best dynamic response; however, this small detector misses much of the beam power.

Next we simulate the same system with the mirror misaligned by 0.025° in the x direction. This small misalignment causes the beam to move approximately 8.7 μm from the ideal detector position. With this shift the 5-μm detector misses almost the entire beam. This can be seen in Fig. 20(b), which shows the BER for this detector to be very high throughout the entire frequency range. However, the most interesting curves in Fig. 20(b) are found for the 10- and the 15-μm detectors. The 10-μm detector also misses much of the propagating beam, and as a result the BER performance is not as good as that in the example above. The 15-μm detector now becomes the best detector to use for lower speeds. At

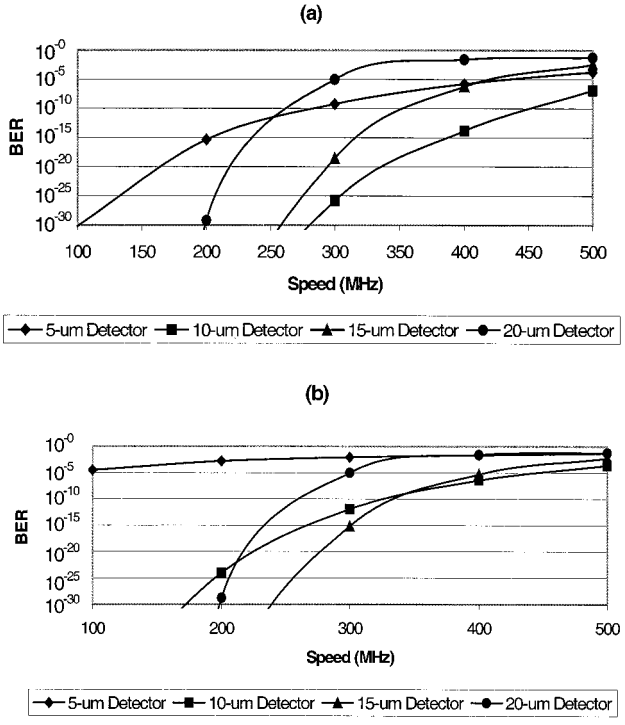

Fig. 20. BER versus the speed trade-off example: (a) No mirror offset. (b) Mirror offset by 0.025°.

approximately 350 MHz the larger capacitance of the 15-μm detector degrades the system performance below that of the 10-μm detector. The 20-μm detector still captures almost the entire offset beam. Therefore the 20-μm curve looks almost exactly the same in both Figs. 20(a) and 20(b).

As expected, for compensating for the possibility of mechanical misalignments in such systems, a larger detector is necessary. However, the large capacitance that is associated with the larger detector degrades the system performance at higher speeds.

We can use Chatoyant not only to simulate simple changes to the device parameters, such as noise, operating speed, and detector size, but we can also easily make changes in the technology chosen for the sources and detectors by simply replacing the icons in the simulation. Further, we can make changes in the architecture of such a system, such as replacing the multifacet mirror with a single mirror and tilted lenses.

5. Summary and Conclusions

We have shown how Chatoyant can be used for the modeling and the simulation of hybrid OE FS systems. We have used analytical, empirical, and lumped-parameter models for OE components and a Gaussian beam propagation model for optical signals. We made a static analysis of systems that showed the effects of detector size, lens misalignment, and clipping. For the dynamic simulations we used a time-domain analysis of the each of the OE components, introduced noise sources, and calculated insertion loss, cross talk, and BER's.

Our system is, to our knowledge, the only system-level simulation tool to date that can model Gaussian optical signal propagation with mechanical toleranc-ing as well as the dynamics of OE components. We have not yet modeled noise in our drivers, sources, or modulators. Additionally, cross talk between electrical signal channels and power supplies is also important. On the other hand, modulation and coding methods, differential signaling, adaptive thresholding, and other techniques are typically used to reduce the BER. Therefore we need to develop models for the effects of these techniques as well.

One of the advantages of building Chatoyant on top of an object-oriented backbone, such as Ptolemy, is that it is modular, that is, users can independently develop their own models as stars, easily integrate them into the existing Chatoyant framework, and perform system-level simulations with our existing model library. Our goal has been to provide the designer with a system-level design environment that can address the mixed-technology concerns of OE system design. With system-level models, designers are able to make the trade-offs, optimizations, and technology choices necessary to realize high-quality FS OE systems without recourse to expensive fabrication, testing, and iteration by using hardware prototypes.

The authors acknowledge the partial support of the U.S. National Science Foundation through grants ECS-9616879, ECS-961739 and the U.S. Defense Advanced Research Project Agency under contract F30602-97-2-0122.

References

1. R. Arrathoon, *Optical Computing, Digital and Symbolic* (Marcel Dekker, New York, 1985).
2. R. A. Athale, ed., *Digital Optical Computing*, Vol. CR35 of SPIE Critical Reviews Series (Society of Photo-Optical Instrumentation Engineers, Bellingham, Wash., 1990).
3. H. S. Hinton, *An Introduction to Photonic Switching Fabrics* (Plenum, New York, 1993).
4. A. D. McAulay, *Optical Computer Architectures* (Wiley, New York, 1991).
5. C. Bergstrom and J. Palais, "Digital fiber optic network synthesis," IEEE Lightwave Telecommun. Syst. **3,** 27–33 (1992).
6. D. Zaleta, S. Patra, V. Ozguz, J. Ma, and S. H. Lee, "Toleranc-ing of board-level free-space optical interconnects," Appl. Opt. **35,** 1317–1327 (1996).
7. J. Fan, B. Catanzaro, F. E. Kiamilev, S. C. Esener, and S. H. Lee, "Architecture of an integrated computer-aided design system for optoelectronics," Opt. Eng. **33,** 1571–1580 (1994).
8. S. Koh and L. Ye, "Modeling and simulation of optoelectronic multichip modules using VHDL," in *Optoelectronic Integrated Circuits*, Y-S. Park, ed., Proc. SPIE **3006,** 418–428 (1997).
9. D. Fey, *HADLOP* (Friedrich-Schiller-Universitat, Jena, Germany, 1996, http://www2.informatik.unijena.de/pope/HADLOP/hadlop.html).
10. M. A. Neifeld and W.-C. Chou, "Electrical packaging impact on source components in optical interconnects," IEEE Trans. Components, Packag. Manuf. Technol. Part B **18,** 578–595 (1995).
11. J. M. Xu and D. S. Ellis, "OE^{UT}-Spice: A CAD tool for design and simulation of OEIC," in *Optoelectronic Integrated Circuits*, Y-S. Park, ed., Proc. SPIE **3006,** 406–417 (1997).
12. J. C. Eble, V. K. De, and J. D. Meindl, "A first generation generic system simulator (GENESYS) and its relation to NTRS," in *Proceedings of the IEEE Eleventh Biennial University/Government/Industry Microelectronics* (*UGIM*) *Symposium* (Institute of Electrical and Electronics Engineers, New York, 1995), pp. 147–154.
13. A. J. Lowery, P. C. R. Gurney, X.-H. Wang, L. V. T. Nguyen, and M. Premartane, "Time-domain simulation of photonic devices, circuits and systems," in *Physics and Simulation of Optoelectronic Devices IV*, W. W. Chow and M. Osinski, eds., Proc. SPIE **2693,** 624–635 (1996).
14. J. J. Morikuni and S. Kang, *Computer-Aided Design of Optoelectronic Integrated Circuits and Systems* (Prentice-Hall, Englewood Cliffs, N.J., 1997).
15. A. Louri and J. Na, "Modeling and simulation methodology for digital optical computing systems," Appl. Opt. **33,** 1549–1558 (1994).
16. A. T. Yang, D. S. Gao, and S. M. Kang, "Computer-aided simulation of optical interconnects for high-speed digital systems," in *Proceedings of the 1988 IEEE International Conference on Computer Design* (IEEE Computer Society, Los Alamitos, Calif., 1988), pp. 87–90.
17. S. P. Levitan, P. J. Marchand, M. Rempel, D. M. Chiarulli, and F. B. McCormick, "Computer-aided design of free-space optoelectronic interconnection (FSOI) systems," in *Second International IEEE Workshop on Massively Parallel Processing Using Optical Interconnections*, E. Schenfeld, ed. (IEEE Computer Society, Los Alamitos, Calif., 1995), pp. 239–245.
18. B. E. A. Saleh and M. C. Teich, *Fundamentals of Photonics* (Wiley, New York, 1991), Chaps. 1–3.

19. S. Chenney, *Sced: Constraints Based Scene Editing User's Guide* (Basser Department of Computer Science, University of Sydney, Sydney, Australia, 1996, http://http.cs.berkeley.edu/~schenney/sced/sced.html).
20. D. Wells and C. Young, *The Waite Group's Ray Tracing Creations* (Waite Group, Corte Madera, Calif., 1993, http://www.povray.org/).
21. P. Belland and J. P. Crenn, "Changes in the characteristics of a Gaussian beam weakly diffracted by a circular aperture," Appl. Opt. **21,** 522–527 (1982).
22. F. B. McCormick, F. A. P. Tooley, T. J. Cloonan, J. M. Sasian, and H. S. Hinton, "Microbeam optical interconnections using microlens arrays," in *Photonic Switching*, H. S. Hinton and J. W. Goodman, eds., Vol. 8 of OSA Proceedings Series (Optical Society of America, Washington, D.C., 1991), pp. 90–96.
23. S. P. Levitan, P. J. Marchand, T. P. Kurzweg, M. A. Rempel, D. M. Chiarulli, C. Fan, and F. B. McCormick, "Computer-aided design of free-space opto-electronic systems," in *Proceedings of the 1997 Design Automation Conference* (Association for Computing Machinery, New York, 1997), pp. 768–773.
24. G. Vdovin, H. van Brug, and F. van Goor, "LightPipes: software for education in coherent optics," presented at the Fifth International Topical Meeting on Education and Training in Optics, Delft, The Netherlands, 19–21 August 1997.
25. C. Fan, B. Mansoorian, D. A. Van Blerkom, M. W. Hansen, V. H. Ozguz, S. C. Esener, and G. C. Marsden, "Digital free-space optical interconnections: a comparison of transmitter technologies," Appl. Opt. **34,** 3103–3115 (1995).
26. O. Kibar, D. A. Van Blerkom, C. Fan, and S. C. Esener, "Power minimization and technology comparisons for digital free-space optoelectronic interconnections," presented at OSA Topical Meeting on Spatial Light Modulators, Lake Tahoe, Nev., March 1997.
27. W. Shockley, "A unipolar field effect transistor," Proc. Inst. Radio Eng. **40,** 1365–1376 (1952).
28. N. H. E. Weste and K. Eshraghian, *Principles of CMOS VLSI Design*, 2nd ed. (Addison-Wesley, Reading, Mass., 1993), Chap. 2.
29. J. Buck, S. Ha, E. A. Lee, and D. Messerschmitt, "Ptolemy: a framework for simulating and prototyping heterogeneous systems," Int. J. Comput. Simulation **4,** 155–182 (1994).
30. T. P. Kurzweg, "A CAD system for modeling free space opto-electronic systems," M.S. thesis (Department of Electrical Engineering, University of Pittsburgh, Pittsburgh, Pa., 1997).
31. J. J. Morikuni, A. Dharchoudhury, Y. Leblebici, and S. M. Kang, "Improvements to the standard theory for photoreceiver noise," J. Lightwave Technol. **12,** 1174–1184 (1994).
32. M. C. Jeruchim, "Techniques for estimating the bit error rate in the simulation of digital communication systems," IEEE J. Sel. Areas Commun. **2,** 153–170 (1994).
33. B. K. Whitlock, "iFrost: a CAD tool for modeling and simulation of optical interconnects," Ph.D. dissertation (School of Engineering, University of Illinois at Urbana-Champaign, Urbana, Ill., 1996).
34. A. V. Krishnamoorthy, T. K. Woodward, K. W. Goossen, J. A. Walker, A. L. Lentine, L. M. F. Chirovsky, S. P. Hui, B. Tseng, R. Leibenguth, J. E. Cunningham, and W. Y. Jan, "Operation of a single-ended 550Mbit/s, 41fJ, hybrid CMOS/MQW receiver-transmitter," Electron. Lett. **32,** 764–766 (1996).